nature communications

Article

https://doi.org/10.1038/s41467-024-55630-y

General synthesis of neighboring dual-atomic sites with a specific pre-designed distance via an interfacial-fixing strategy

Received: 11 January 2024

Accepted: 17 December 2024

Published online: 02 January 2025

Check for updates

Yan Yan[1], Rui Yu[1], Mingkai Liu[1] ✉, Zehua Qu[2], Jifeng Yang[1], Siyuan He[1], Hongliang Li[3] ✉ & Jie Zeng[1,3] ✉

A potential non-precious metal catalyst for oxygen reduction reaction should contain metal-N_4 moieties. However, most of the current strategies to regulate the distances between neighboring metal sites are not pre-designed but depend on the probability by tuning the metal loading or the support. Herein, we report a general method for the synthesis of neighboring metal-N_x moieties (metal = Fe, Cu, Co, Ni, Zn, and Mn) via an interfacial-fixing strategy. Specifically, polydopamine is used to coat nanotemplates made of metal oxides, followed by pyrolysis to form a metal-oxide skeleton coated by rich nitrogen-doped carbon shells. After chemically etching the skeleton, only interfacial metal atoms strongly bonded with the support via nitrogen atoms are retained. The high purity (>95%) of dual Fe sites was confirmed by both the direct visualization of local regions and the indirect evidence of the averaged information. When these neighboring metal-N_x moieties are applied for oxygen reduction reaction, Fe-N_x moieties exhibit the superior activity, even outperforming commercial Pt/C in the aspects of the half-wave potential, methanol tolerance, carbon monoxide tolerance, and robustness.

As the cathodic process of metal-air batteries and fuel cells, the oxygen reduction reaction (ORR) has garnered intensive attention, especially for searching nonprecious metals to replace platinum-based electrocatalysts. Nature routinely performs the reduction of O_2 using a metalloenzyme named as cytochrome c oxidase, which only contains non-precious metals such as iron and copper[1]. Specifically, the active center within the cytochrome c oxidase comprises an iron heme, a distal copper in close proximity (0.5 nm) to iron heme, and surrounding organic ligands[1]. A promising non-precious metal catalyst for ORR should contain metal (M)-N_4 moieties in close proximity rather than isolated sites. A typical approach to fabricating neighboring metal sites is based on increasing the metal loading in single-atom catalysts, following the probability that the higher the metal loading the closer the neighboring metal atoms[2–4]. Up to date, great efforts have been made to improve the metal-atom densities in single-atom catalysts[5–13]. For instance, a two-step annealing method prevents thermally induced aggregation of single atoms via stepwise ligand removal, resulting in a high metal loading of up to 23 wt%[14]. When graphene quantum dots, later interweaved into a carbon matrix, were used as a support, the numerous anchoring sites on the support facilitate the generation of high densities of transition-metal atoms up to 40 wt%[15]. Apart from varying the metal loading, other strategies for the precise fabrication of dual metal sites are mainly dependent on the coordination structures of the support. For example, the synthesis of Fe-Co dual sites was mainly based on the subtle selection of the support, Zn/Co bimetallic MOF, which encapsulated the Fe^{3+} moieties in the cavities via the

[1]Anhui University of Technology, Ma'anshan, Anhui 243002, P. R. China. [2]State Key Laboratory of Molecular Engineering of Polymers, Department of Macromolecular Science, Fudan University, Shanghai 200433, China. [3]Hefei National Research Center for Physical Sciences at the Microscale, Key Laboratory of Strongly-Coupled Quantum Matter Physics of Chinese Academy of Sciences, Key Laboratory of Surface and Interface Chemistry and Energy Catalysis of Anhui Higher Education Institutes, Department of Chemical Physics, University of Science and Technology of China, Hefei, Anhui 230026, P. R. China. ✉e-mail: liumingkai@ahut.edu.cn; lihl@ustc.edu.cn; zengj@ustc.edu.cn

sodalite coordination of Co^{2+} and Zn^{2+} nodes with 2-methylimidazole[16]. The formation of neighboring Fe atoms relied on the presence of vacancies (holes) which provided space to accommodate metal atoms[17]. The recent preparation of well-defined dual metal sites through in situ conversion of nanoparticles also relied on the special support comprising double carbon vacancies which could capture the evaporated metal atoms[18]. However, it remains a grand challenge of precisely tuning the anchoring sites on the support, leading to great difficulties in tuning the types of dual metals (limited by the host metal) and the distance between them (due to the uncontrollable adjacent defects).

Different from the previous works, we circumvented the selection of the support and turned to the metals themselves by making use of the original crystal structures for tuning the proximity of metal sites. Herein, we report a general method for fabricating neighboring M-N_x moieties (M = Fe, Cu, Co, Ni, Zn, and Mn) with specific distances via an interfacial-fixing strategy. We use Fe as the representative metal center to demonstrate our synthetic strategy. Specifically, polydopamine (PDA) was used as the confined matrix to coat Fe_2O_3 hollow nanotubes, followed by pyrolysis to form a Fe_3O_4 skeleton coated by rich nitrogen-doped carbon shells (Fig. 1a). The lattice of Fe_3O_4 crystals is expected to ensure the arrangement of Fe atoms at the interface. After chemically etching the skeleton, only interfacial Fe atoms strongly bonded with the support were retained. In contrast with traditional etching methods for the synthesis of single-atom catalysts, our strategy used additional urea to provide sufficient nitrogen atoms as a glue to anchor interfacial Fe atoms, even neighboring ones. Both the direct visualization of local regions and the indirect evidence of the averaged information confirm the high purity (>95%) of dual Fe sites. We successfully extended this synthetic method to fabricate various non-precious metal atom pairs including Cu, Co, Ni, Zn, and Mn. As expected, the distances between the atom pairs were consistent with those of their metal oxide counterparts. When we applied these neighboring M-N_x moieties, e.g. Fe_2-N_6, for ORR, Fe_2-N_6 exhibited the superior activity, outperforming commercial Pt/C in terms of the half-wave potential, methanol tolerance, CO tolerance, and robustness. Based on theoretical calculations, the enhanced ORR activity of Fe_2-N_6 derives from the parallel adsorption of O_2 which induces efficient orbital overlap via both σ bonds and π bonds. Moreover, we integrated this catalyst into a Zn-air battery which exhibited the maximum power density of 190.6 mW cm^{-2} at 287.8 mA cm^{-2}, outperforming the Zn-air battery with commercial Pt/C (151.7 mW cm^{-2}, 239.8 mA cm^{-2}).

Results

Synthesis of neighboring Fe atoms

A reported hydrothermal method was employed to synthesize Fe_2O_3 hollow nanotubes. The phase of Fe_2O_3 was confirmed by X-ray diffraction (XRD) pattern (Supplementary Fig. 1). Scanning electron microscopy (SEM) images showed that these nanotubes took an average length of ~260 nm and an outer diameter of ~80 nm (Supplementary Fig. 2). After being coated with a thin layer of PDA, the hollow tube-like structure was perfectly maintained without the aggregation of PDA. Additional urea was used as a nitrogen resource to increase the nitrogen content in the final products. The obtained sample was denoted as Fe_2O_3@PDA composites (Supplementary Fig. 3). It is worth noting that the amount of PDA plays an important role in the shape of Fe_2O_3@PDA composites. Afterwards, Fe_2O_3@PDA composites were carbonized in a tube furnace under Ar at 700 °C for 2 h. The XRD pattern of the pyrolyzed product indicated a typical phase of Fe_3O_4, thereby denoting the sample as Fe_3O_4@C (Supplementary Fig. 1). Finally, Fe_3O_4@C was etched by 4 M HCl solution for 72 h to remove the metal oxide bulks and 1 M H_2SO_4 for 12 h to remove the unstable metal species that anchored on the carbon interfaces. After chemical etching, a double-layer hollow carbon tube was obtained as evidenced by the transmission electron microscopy (TEM) and SEM images (Fig. 1b and Supplementary Fig. 4). As such, the removal of the Fe_3O_4 skeleton did not induce the collapse of the shape in double-layer hollow tubes. The varied contents of N species were shown in Supplementary Table 1. Pure N-C obtained from carbonized PDA contained the same amount of nitrogen as that of Fe_1-N_4 (5.1 wt%), which was lower than that (9.2 wt%) of Fe_2-N_6. As such, additional urea molecules contribute 4.1 wt% of nitrogen-containing to the Fe_2-N_6 sample. According to the XRD pattern of resulted product, a broad diffraction peak appeared at approximately 25° (Supplementary Fig. 5), corresponding to the {002} plane of typical amorphous carbon[19–23]. No other sharp peaks for the phases of iron oxides or carbides were detected, indicating the complete removal of Fe_3O_4 crystals. It is expected that the remaining Fe atoms after etching can retain the arrangement of initial Fe_3O_4 crystals in order to obtain neighboring Fe atoms. The verification of this expectation needs further characterizations at the atomic level. A schematic process was provided to illustrate the conversion of PDA/urea to N-doped carbon layers (Supplementary Fig. 6).

Characterizations of neighboring Fe-N_x moieties

Figure 1c,d shows a high-angle annular dark-field scanning transmission electron microscope (HAADF-STEM) image and the corresponding energy-dispersive X-ray spectroscopic (EDS) mapping analysis. According to these images, C, N, and Fe elements were uniformly distributed throughout the entire double-layer hollow carbon tubes. High-resolution TEM (HRTEM) images showed the absence of Fe clusters or nanoparticles on the support (Supplementary Fig. 7). TEM image observed from the top view further supported the double layer structure of the carbon matrix (Supplementary Fig. 8). In addition, the mass loading of Fe was 2.36 wt% based on inductively coupled plasma-optical emission spectrometry (ICP-OES). As revealed by bright spots and yellow dotted rectangles in Fig. 1e, highly dense pairs of Fe atoms were dispersed on the support (Supplementary Fig. 9). Further observations in the magnified HAADF-STEM image and the corresponding three-dimensional (3D) atom-overlapping Gaussian-function fitting mappings identified the exact distance between two neighboring Fe atoms (Fig. 1f,g and Supplementary Fig. 10). We further collected the distances between neighboring Fe atoms from thousands of objects, obtaining a distance distribution with the majority at 0.29 nm (Fig. 1h), indicating the successful controlling the distance between neighboring Fe atoms in a narrow distribution. A typical pair of neighboring Fe atoms with a distance of 0.29 nm was exemplified by the HAADF-STEM image and the signal intensities in the corresponding region (the inset images in Fig. 1h).

In a unit cell of the Fe_3O_4 crystal, there are four types of distances between Fe atoms, including 2.96, 3.48, 5.13, and 5.93 Å (Fig. 1i). In the preparation process, urea was chosen as the chemical ligand to anchor Fe atoms. The distance between two N atoms in a urea molecule is 2.73 Å. As such, urea can efficiently connect neighboring Fe atoms that are separated near this distance (2.73 Å), that is the nearest pair of Fe atoms with a distance of 2.96 Å. The main distance between neighboring Fe atoms is about 0.29 nm (Fig. 1h). Notably, the experimental distance is slightly shorter than the theoretical value (2.96 Å) of the crystal model, because the ligand with even shorter distance (2.73 Å) between nitrogen anchoring sites induced the contraction of Fe atom pairs on the surface of the Fe_3O_4 crystal. As for the pair of Fe atoms with a distance of 3.48 Å, they are separated too far to be fixed by one urea molecule. These Fe atoms might be coordinated with N atoms of different adjacent urea molecules. During the etching process, these Fe atoms bonded by different urea molecules are likely to be separated apart further than the theoretical distance of 3.48 Å, so that the characteristic distance (3.48 Å) cannot be well maintained. The possibility of this situation is much smaller than that linked by one urea molecule. As such, we observed a weak wide peak at around 0.35 nm in Fig. 1h. With regard to the pairs of Fe atoms with distances of 5.13 and 5.93 Å,

https://doi.org/10.1038/s41467-024-55630-y

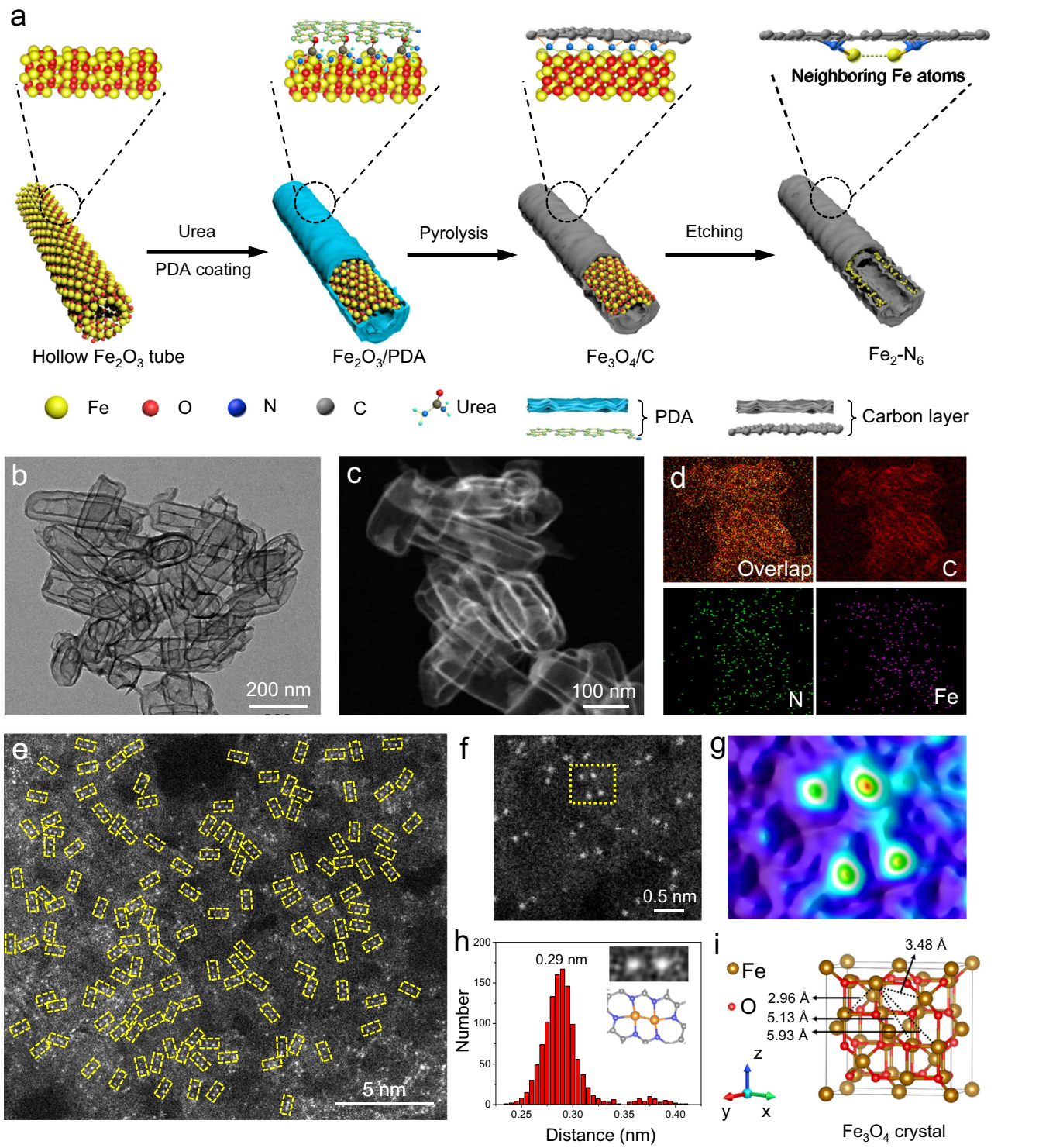

Fig. 1 | Synthesis and structural characterizations. a Schematic illustration of the synthesis of Fe_2-N_6. **b** TEM, (**c**) HAADF-STEM, and (**d**) EDS elemental mapping images of Fe_2-N_6. **e** Aberration-corrected HAADF-STEM image of Fe_2-N_6. **f** Magnified HAADF-STEM image of Fe_2-N_6 and (**g**) the corresponding 3D atom-overlapping Gaussian-function fitting maps of the region in panel **f**. **h** Distance distribution between neighboring Fe atoms. The inset images in panel **h** show the HAADF-STEM image and the proposed model of a typical pair of neighboring Fe atoms. **i** Crystal structure of Fe_3O_4.

both of them have adjacent Fe atoms with the distance of 2.96 Å, as discussed in the first situation. As such, these pairs of Fe atoms were just synthesized as designed instead of being distributed randomly. Moreover, we define the pair of Fe atoms (Fe_2-N_6) that can be most efficiently anchored by the urea ligand as neighboring Fe atoms. These Fe atoms are separated at a distance of about 0.29 nm. The Fe atoms with longer distances are denoted as isolated Fe atoms. We used this definition because the distance between these neighboring atoms could be facilely tuned, whereas the distances between other Fe atoms were largely dependent on the possibility. The content of neighboring Fe atoms in Fe_2-N_6 was as high as 98%, indicating the high purity of dual atom pairs (Supplementary Fig. 11). Intriguingly, heavy carbon layers resulting from the double usage of dopamine also achieved the formation of neighboring Fe sites (Supplementary Figs. 12 and 13).

For comparison, we prepared a reference sample with the Fe mass loading of 0.32 wt% using the same procedure except for not adding additional urea. The overall morphology also exhibited a double-layer hollow tube (Supplementary Fig. 14). The XRD pattern showed the existence of typical amorphous carbon without any iron-related phases (Supplementary Fig. 15). As shown in Supplementary Fig. 16, a and b, the distance between Fe atoms ranged from 0.45 to 0.82 nm, significantly longer than that of neighboring Fe atoms. These Fe atoms were featured as isolated ones. A typical HAADF-STEM image and its line-scanning intensity profile of isolated Fe atoms revealed a distance of 0.60 nm which was longer than 0.29 nm for neighboring ones (Supplementary Fig. 16, c and d). Therefore, the introduction of urea leads to the stabilization of neighboring Fe atoms which are presumably coordinated with N atoms. This point was supported by N 1*s* X-ray photoelectron spectroscopy (XPS) analysis. For both isolated and neighboring Fe atoms, various N-containing species were identified, including oxidized N, graphitic-N, pyrrolic-N, pyridinic-N, and Fe-N (Supplementary Fig. 17a). The content of Fe-N in neighboring Fe atoms was 0.81 wt%, higher than that (0.23 wt%) in isolated ones (Supplementary Fig. 17b), verifying the more efficient stabilization of neighboring Fe atoms by N atoms. In addition, we took metallic Fe as the metal source to prepare single metal atoms, while other experimental details were the same as those for the preparation of Fe_2-N_6. However, no isolated metal sites were obtained (Supplementary Fig. 18). It can be ascribed to the reason that the zero-valence Fe atoms in metallic Fe are reluctant to coordinate with N atoms in urea. Thus, a basic requirement is that the metal source should strongly interact with the ligand. To investigate the role of ligand, we replaced urea with ethanediamine. It is found that the distance between Fe atoms became wider ranging from 0.27 to 0.39 nm (Supplementary Fig. 19). This is because ethylenediamine is a flexible molecule, of which distance between the two N atoms on the carbon chain can easily change, making it difficult to fix the distance between two Fe atoms. We tried another ligand, thiourea, which possesses a similar structure to that of urea. The use of thiourea ligand also led to the formation of neighboring metal atoms with the possible involvement of both N and S in the coordination configuration (Supplementary Fig. 20). Therefore, the successful preparation of dual Fe atoms lies in the perfect match of the ligand and the lattice of the template.

To investigate the coordination structures of isolated and neighboring Fe atoms, we carried out X-ray absorption near-edge structure (XANES) and extended X-ray absorption fine structure (EXAFS) measurements. The absorption threshold positions of both neighboring and isolated Fe atoms were located between Fe_2O_3 and Fe_3O_4, suggesting that the valence state of Fe atoms was between +2 and +3 (Supplementary Fig. 21a)[24]. Notably, the calculated XANES spectrum of the Fe_2-N_6 model exactly reproduced the experimental spectrum of Fe_2-N_6 (Supplementary Fig. 22). As shown in EXAFS and the corresponding fitting results, neighboring Fe atoms exhibited a strong peak for the Fe-N shell with a bond length (*R*) of 1.90 Å and a coordination number (*CN*) of 2.8 (Supplementary Fig. 21b and S23a, Supplementary Table 2). Another prominent peak corresponded to the Fe-Fe contribution with *R* of 2.62 Å and *CN* of 0.9 (Supplementary Fig. 21b and S23a, Supplementary Table 2). The near unit *CN* for Fe-Fe bonds was a typical characteristic of atom pairs[25–27]. As such, we denoted neighboring Fe atoms as Fe_2-N_6 (Supplementary Fig. 23b). For isolated Fe atoms, only the peak for Fe-N bonds was observed with *R* of 1.84 Å and *CN* of 3.8, denoting this sample as Fe_1-N_4 (Supplementary Fig. 21b and S24, Supplementary Table 2).

Moreover, we conducted N and O K-edge soft XANES measurements of Fe_2-N_6, Fe_1-N_4, and carbon matrix. As shown in N K-edge XANES spectra (Supplementary Fig. 25a), obvious absorption at 400.5 eV appeared for Fe_2-N_6 and Fe_1-N_4, corresponding to the Fe-N bonding based on the previous papers[28]. This absorption was absent for the carbon matrix. As such, there existed Fe-N bonds in both Fe_2-N_6 and Fe_1-N_4. The O K-edge XANES spectra of these three samples were similar, showing a prominent peak at 532.8 eV for the π* state of C = O bonds (Supplementary Fig. 25b)[29]. This result implies that the existing O species were bonded with the carbon matrix rather than coordinated with Fe atoms. As a result, the Fe atoms were only coordinated by N atoms. This result also corresponded to the synthetic procedure. Specifically, urea was used as a coating layer which was inserted between the Fe_2O_3 template and the PDA layer. Fe atoms on the surface of Fe_2O_3 and Fe_3O_4 were preferentially coordinated with N atoms in urea molecules. Meanwhile, the chemical bonds between O and Fe atoms in Fe_3O_4 crystal were broken down when they underwent strong chemical etching (by 4 M HCl solution for 72 h and 1 M H_2SO_4 for 12 h). As such, it is reasonable that O atoms did not take part in the coordination with Fe atoms in Fe_2-N_6 but existed on the carbon matrix.

Actually, the evidence of HAADF-STEM images is not convincing enough to quantify the purity of neighboring Fe atoms, since it only reflects the local information. To this end, we conducted temperature-programmed desorption (TPD) measurements with mass spectroscopy (MS) using acetylene (C_2H_2) as a probe molecule to quantify the averaged purity of neighboring Fe atoms. Since the adsorption strength of acetylene molecules on isolated Fe sites differs from that on dual Fe sites, the temperatures for the desorption of acetylene molecules from isolated and dual Fe sites should be different. We analyzed the data in Supplementary Fig. 26a, b. The C_2H_2-TPD-MS profile of Fe_1-N_4 shows a symmetric peak at 103.2 °C which we assigned to the adsorption on isolated Fe sites. As for the C_2H_2-TPD-MS profile of Fe_2-N_6, the peak was shifted to a higher temperature. This phenomenon is rational since the adsorption on dual Fe sites is stronger than that on isolated sites. Specifically, the acetylene molecule is physically adsorbed on Fe_1-N_4 with an adsorption energy (E_{ads}) of -0.542 eV (Supplementary Fig. 26c). As for Fe_2-N_6, the acetylene molecule is adsorbed via a flat-lying bidentate configuration, with an E_{ads} of -1.620 eV, where the C-C bond was stretched to 1.306 Å (Supplementary Fig. 26d). Moreover, the shape of this peak was asymmetric, indicating the existence of more than one peak. In this work, we attributed the other peak to that for isolated Fe sites. As such, we adopted the temperature of 103.2 °C for isolated Fe sites and the peak temperature of 123.6 °C to fit the profile of Fe_2-N_6. The latter we assigned to the adsorption on dual Fe sites. As shown in the fitting profile of Fe_2-N_6, the peak area ratio of dual Fe sites to isolated Fe sites was 10.6:1 (Supplementary Fig. 26b). When we assume that one Fe site adsorbs one acetylene molecule, the purity of dual sites in the Fe_2-N_6 sample was 91.4%. Actually, it is more rational that one isolated Fe site adsorbs one acetylene molecule via an end-on mode, while a pair of dual Fe sites adsorb one acetylene molecule via a bidentate mode. In other words, for dual sites, one acetylene molecule corresponds to two Fe atoms. Thus, the purity of dual sites in the Fe_2-N_6 sample should be 95.5%, close to the value (98%) from the statistics of HAADF-STEM images. Overall, both the direct visualization of local regions and the indirect evidence of the averaged information confirm the high purity (>95%) of dual Fe sites in Fe_2-N_6.

In addition, we adjusted the amount of urea added during the synthesis process and measured the Fe loading and the distance between Fe atoms. As the amount of urea increased from 10 to 100 mg, the Fe loading increased from 0.55 to 2.36 wt%, while the distance between iron atoms decreased from 0.54 to 0.29 nm, with the distribution of distances between Fe atoms becoming more concentrated (Supplementary Fig. 27). When the amount of urea exceeded 100 mg (*e.g.*, 120 mg), the Fe loading and the distance between iron atoms remained largely unchanged at 2.37 wt% and 0.29 nm, respectively, due to saturation (Supplementary Fig. 28). Also, we tuned the pyrolysis temperature to minimize the decomposition loss of urea molecules while ensuring the occurrence of the pyrolysis reaction. we lowered the pyrolysis temperature to 500 °C and reduced the urea content to 50 mg (see Supplementary Table 3 for synthesis condition

https://doi.org/10.1038/s41467-024-55630-y

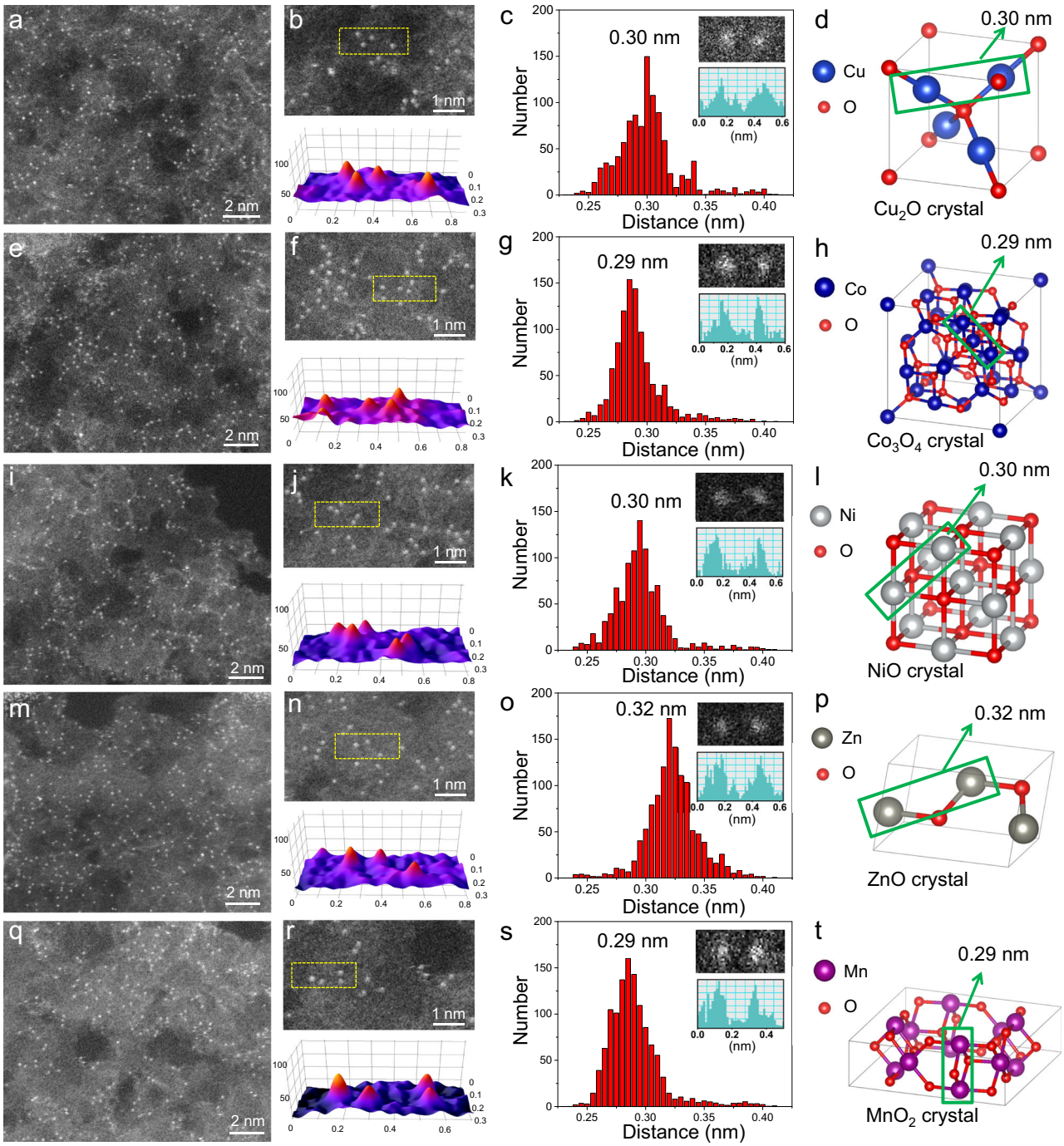

Fig. 2 | Structural characterizations of different neighboring M-N_x moieties. Aberration-corrected HAADF-STEM images of neighboring (**a**) Cu-N_x, (**e**) Co-N_x, (**i**) Ni-N_x, (**m**) Zn-N_x, and (**q**) Mn-N_x moieties. Enlarged HAADF-STEM images and corresponding 3D atom-overlapping Gaussian-function fitting maps of neighboring (**b**) Cu-N_x, (**f**) Co-N_x, (**j**) Ni-N_x, (**n**) Zn-N_x, and (**r**) Mn-N_x moieties. Distance distribution between neighboring (**c**) Cu-N_x, (**g**) Co-N_x, (**k**) Ni-N_x, (**o**) Zn-N_x, and (**s**) Mn-N_x moieties. Crystal structures of (**d**) Cu_2O, (**h**) Co_3O_4, (**l**) NiO, (**p**) ZnO, and (**t**) MnO_2.

comparison). The Fe content in the synthesized sample was reduced to 1.62%, while maintaining high Fe diatomic purity (Supplementary Fig. 29). Notably, the Fe content of 1.62% at a pyrolysis temperature of 500 °C was higher than that (1.32%) at 700 °C, implying that lowering the pyrolysis temperature indeed decreased the loss of urea molecules and thereby increased the amount of anchored Fe atoms.

Synthesis of other neighboring M-N_x moieties

To explore whether our interfacial-fixing method can be extended to prepare other neighboring M-N_x moieties, we used Cu_2O as the substrate to synthesize neighboring Cu-N_x moieties. Multi-scale characterization evidence ranging from subnanometers to millimeters was integrated to exclude the existence of clusters or nanoparticles (Supplementary Fig. 30). To quantify the distance between neighboring Cu atoms, we conducted aberration-corrected HAADF-STEM images (Fig. 2a). Magnified HAADF-STEM image and the corresponding 3D atom-overlapping Gaussian-function fitting mappings identified the exact distance between two neighboring Cu atoms (Fig. 2b). The main distance between adjacent Cu atoms was determined to be 0.30 nm (Fig. 2c), which is consistent with the distance between two Cu atoms

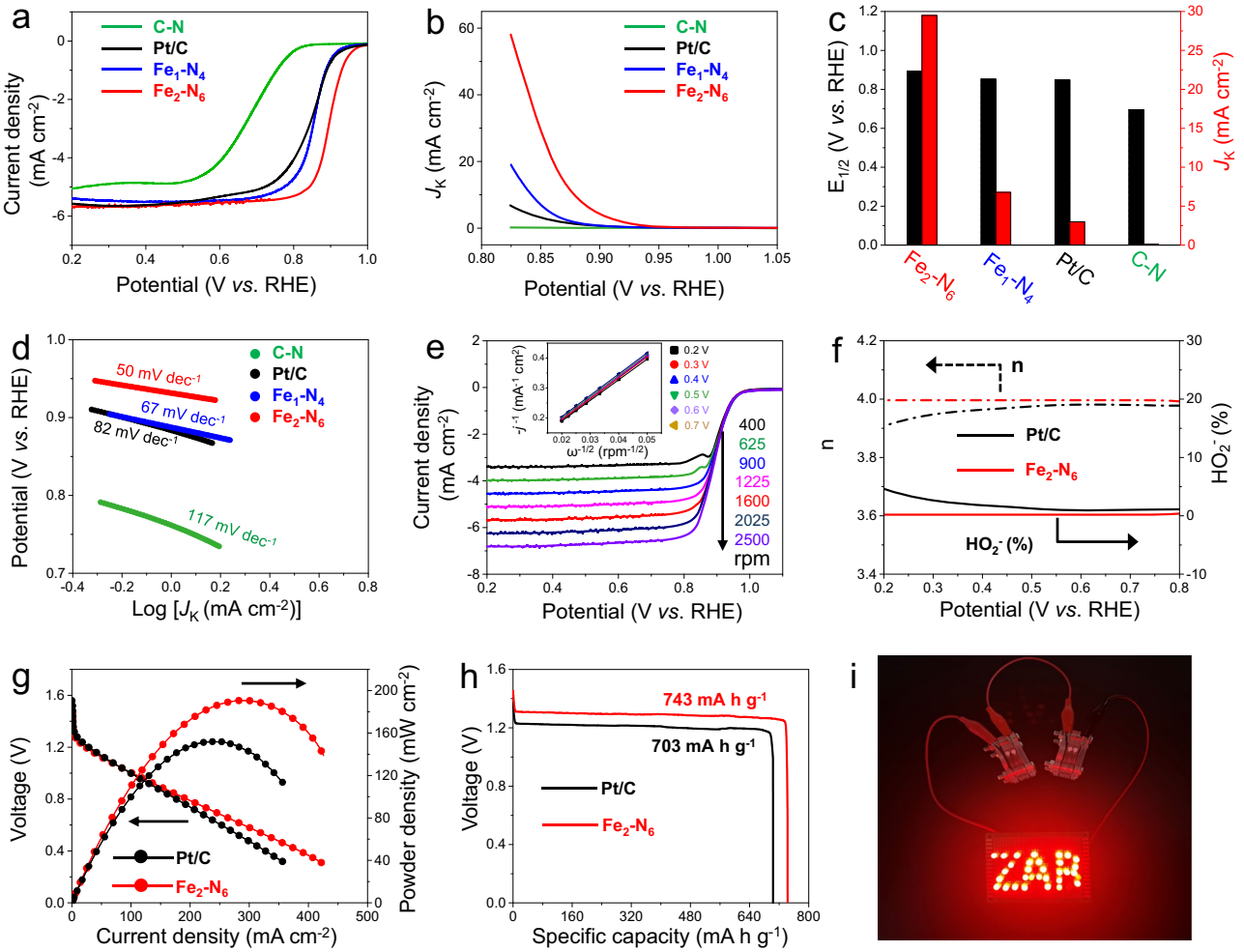

Fig. 3 | ORR properties. a Linear sweep voltammetry curves, **b** kinetic current density curves, (**c**) $E_{1/2}$ and J_k, and (**d**) corresponding Tafel plots of Fe_2-N_6, Fe_1-N_4, commercial Pt/C, and C-N matrix. **e** LSV curves of Fe_2-N_6 in O_2-saturated 0.1 M KOH with various rotating rates. **f** Electron transfer number (n) and peroxide species yield of Fe_2-N_6 and commercial Pt/C. **g** Discharge polarization curves and corresponding power density curves of the aqueous Zn-air batteries using Fe_2-N_6 and commercial Pt/C as air electrode. **h** Galvanostatic discharge curves of Zn-air batteries with Fe_2-N_6 and commercial Pt/C as an air electrode at a current density of 2 mA cm^{-2}. **i** Photograph of lit red LED display powered by Zn-air batteries with Fe_2-N_6 air electrode.

in the Cu_2O crystal (Fig. 2d). These results demonstrate the successful synthesis of neighboring Cu-N_x moieties with presupposed distances.

Other non-precious metal moieties, including Co, Ni, Zn, and Mn were also fabricated via the same synthetic method. The absence of clusters or nanoparticles was confirmed by a series of characterizations (Supplementary Fig. 31-35). As shown in Fig. 2e-t, the distances between neighboring metal atoms were all consistent with those of their metal-oxide counterparts. These results confirm the generality of our synthetic strategy for neighboring M-N_x moieties.

ORR performance

In order to evaluate the enhancement of catalytic capability by the achieved neighboring single atoms, Fe_2-N_6 and Fe_1-N_4 were explored toward ORR in a three-electrode system. Similar specific surface area and porosity of Fe_1-N_4 and Fe_2-N_6 can exclude the differences in catalytic performance that resulted from the pore structure (Supplementary Fig. 36 and Supplementary Table 4). Moreover, the porous structure can ensure the fully exposure of Fe atoms, which can be utilized during the ORR process. ORR activities were investigated by cyclic voltammetry (CV) measurements in O_2 and N_2 saturated KOH solution (0.1 M). The peak potential of Fe_2-N_6 was 0.92 V *vs.* reversible hydrogen electrode (RHE), more positive than that (0.87 V) of Fe_1-N_4 (Supplementary Fig. 37). The ORR activities were also evaluated by rotating disk electrode (RDE) measurements with a rotating rate of 1600 rpm. The linear sweep voltammetry (LSV) results indicated that Fe_2-N_6 achieved the good ORR catalytic activities with an onset potential (0.95 V) and the most positive half-wave potential (0.90 V), outperforming those of Fe_1-N_4 (0.91 V and 0.86 V) and commercial Pt/C catalysts (0.92 V and 0.85 V) (Fig. 3a). In order to quantitatively assess the ORR activity, the kinetic current density (J_k) was calculated based on the LSV curves in Fig. 3a. Figure 3b exhibited the whole kinetics control and mixed kinetics-diffusion control regions of the catalysts. J_k of Fe_2-N_6 was apparently higher than those of the other three samples at 0.92 - 0.82 V. Specifically, at 0.85 V, the J_k value of Fe_2-N_6 reached 29.4 mA cm^{-2}, being 4.2 and 9.9 times higher than that of Fe_1-N_4 (7.02 mA cm^{-2}) and that of commercial Pt/C (2.98 mA cm^{-2}), respectively (Fig. 3c). Strikingly, the Fe_2-N_6 catalyst exhibited the lowest Tafel slope (50 mV·dec^{-1}) (Fig. 3d) compared with Fe_1-N_4 (67 mV dec^{-1}) and Pt/C (82 mV dec^{-1}). According to electrochemical impedance spectroscopy (EIS), Fe_2-N_6 and commercial Pt/C showed the smallest charge transfer resistance among the samples (Supplementary Fig. 38), resulting in the fast reaction kinetics of Fe_2-N_6 catalyst. Considering the difference in Fe contents between Fe_2-N_6 and Fe_1-N_4, we mixed Fe_2-N_6 with the C-N matrix in an electrode to ensure the same content of Fe atoms in the prepared electrode as that in Fe_1-N_4 (see details in the experimental section). In spite of the same content of Fe,

Fe_2-N_6/C-N still exhibited a higher $E_{1/2}$ (0.88 V vs. RHE) value than that (0.86 V vs. RHE) of Fe_1-N_4 (Supplementary Fig. 39). As such, the dual Fe pairs were intrinsically more active than isolated Fe sites during ORR. The ORR performance of Fe_2-N_6 surpassed most of the reported Fe-based catalysts (Supplementary Fig. 40 and Supplementary Table 5). Moreover, Fe_2-N_6 also outperformed other neighboring M-N_x (M = Cu, Co, Ni, Zn, and Mn) moieties (Supplementary Fig. 41). Therefore, Fe_2-N_6 possessed a superior ORR activity compared with commercial Pt/C in an alkaline medium.

The reaction kinetics were further explored. Figure 3e shows the LSV curves of Fe_2-N_6 at different rotating rates. The current densities of catalysts were obviously enhanced with the increase in rotational speeds. The Koutechy-Levich (K-L) plots derived from the LSV curves of Fe_2-N_6 showed high linearity in the potential range of 0.2 to 0.7 V, implying first-order reaction kinetics for ORR (the inset of Fig. 3e). Based on the K-L plots, the electron transfer numbers (n) for Fe_2-N_6 at different potentials approached to the theoretical value of 4, indicating that the ORR proceeded mainly in a four-electron reduction process. Additionally, K-L plots of Fe_1-N_4 exhibited electron transfer numbers of 3.85-3.96 (Supplementary Fig. 42), while the carbon matrix achieved electron transfer numbers of 3.82-3.87 (Supplementary Fig. 43). To support the above results, we further measured the yields of peroxide species. In the rotating ring disk electrode (RRDE) tests, the yield of peroxide species for Fe_2-N_6 was fairly low (<1.0%) (Fig. 3f). The electron transfer number (n) was calculated at around 4 (Fig. 3f), consistent with the results from the K-L plots. In comparison, the yields of peroxide species for Fe_1-N_4 and carbon matrix were higher than that for Fe_2-N_6 at the applied potentials, exhibiting the n values of 3.79-3.87 and 3.69-3.81, respectively (Supplementary Fig. 44).

We further evaluated the ORR stability of Fe_2-N_6 in comparison with commercial Pt/C in O_2-saturated 0.1 M KOH solution. As shown in Supplementary Fig. 45, the Fe_2-N_6 still maintained 97% of its initial current after 10,000 s, whereas commercial Pt/C maintained only 85% of the initial current. These results revealed a high stability of Fe_2-N_6. In methanol fuel cells, the tolerance to methanol crossover is of great importance for practical applications, as the efficiency of commercial Pt/C is generally degraded by the presence of methanol in the electrolyte. The methanol tolerance of Fe_2-N_6 was evaluated by injecting a methanol solution during the chronoamperometric measurement. After the addition of methanol, Fe_2-N_6 still maintained a stable current density with negligible fluctuation, whereas the current of commercial Pt/C catalyst decreased to less than 70% (Supplementary Fig. 46). These results demonstrate that Fe_2-N_6 possessed high tolerance to methanol crossover. CO tolerance performance of Fe_2-N_6 and Pt/C was further evaluated. Compared with Pt/C, Fe_2-N_6 was much more tolerant against CO poisoning (Supplementary Fig. 47), while the advantage of Fe_2-N_6 became more prominent with the extension of reaction time (see detailed analysis in the Note of Supplementary Table 6). Moreover, the long-term durability of Fe_2-N_6 in the practical environment was conducted according to an accelerated durability test (ADT). As shown in Supplementary Fig. 48, a small $E_{1/2}$ decay (10 mV) of Fe_2-N_6 was observed even after 50,000 ADT cycles, smaller than those of Fe_1-N_4 (36 mV) and commercial Pt/C (55 mV), revealing outstanding long-term durability of Fe_2-N_6 for ORR.

To demonstrate the potential application of Fe_2-N_6, we constructed Zn-air batteries using Fe_2-N_6 as the air cathode and Zn foil as the anode. 6 M KOH aqueous solution with 0.2 M zinc acetate was used as the electrolyte. The Zn-air batteries based on Fe_2-N_6, Fe_1-N_4 and commercial Pt/C exhibited open circuit voltage of 1.425, 1.380 and 1.410 V, respectively (Supplementary Fig. 49). The maximum power density reached 190.6 mW cm^{-2} at a current density of 287.8 mA cm^{-2} (Fig. 3g), which was much higher than that of the Pt/C-based Zn-air battery (151.7 mW cm^{-2}, 239.8 mA cm^{-2}). The calculated specific capacities of Fe_2-N_6-based Zn-air battery achieved a high value of 743 mA h g^{-1} at 2 mA cm^{-2} (Fig. 3h), which was larger than that of commercial Pt/C (703 mA h g^{-1}). Moreover, a mini fan and a red light-emitting diode (LED) can be powered by two Fe_2-N_6-based Zn-air batteries (Fig. 3i, Supplementary Movies 1 and 2). These results demonstrate the superior catalytic activities of Fe_2-N_6 for ORR. Rechargeable Zn-air batteries with Fe_2-N_6, Fe_1-N_4 and commercial Pt/C acting as cathodes were also assembled, where Fe_2-N_6 were stably cycled up to 70 h, much more stable than Fe_1-N_4 and commercial Pt/C (Supplementary Fig. 50).

In order to meet the increasing demand for wearable electronics, we further tested whether Fe_2-N_6 could be used as a cathode for fabricating flexible Zn-air batteries with Zn foil as an anode and alkaline polyvinyl alcohol gel solid-state as an electrolyte (Supplementary Fig. 51a). This flexible Zn-air battery exhibited a stable open-circuit voltage of ~1.47 V (Supplementary Fig. 51b). A red LED was lit up by both flat and bend Zn-air batteries (Supplementary Fig. 51c). The charge and discharge platforms were well maintained by alternative changing the Fe_2-N_6-based battery between flat and bend states (Supplementary Fig. 51d). These results confirm the remarkable electrochemical performance of the Fe_2-N_6 catalyst as a flexible air electrode. HAADF-STEM image of prepared Fe_2-N_6 catalyst after long-term cycling showed the preservation of Fe atom pairs, suggesting the robustness of this catalyst (Supplementary Fig. 52).

DFT studies

To further scrutinize the ORR mechanism, we conducted density functional theory (DFT) calculations. Various reported literature that contained theoretical calculations of ORR over Fe-based catalysts demonstrated that the activation of O = O double bonds was the rate determining step[30,31]. Taking these papers as reference, we used the cleavage of O = O bonds as the descriptor to evaluate the catalytic properties of the developed catalysts. The adsorption configurations of oxygen molecules on Fe_1-N_4 and Fe_2-N_6 were built. Specifically, Fe_1-N_4 adopts the end-on adsorption of O_2 (Fe_1-N_4-O_2) with an adsorption energy (E_{ads}) of -2.929 eV and an O-O bond length of 1.294 Å (Fig. 4a, Supplementary Data 1). As for Fe_2-N_6, the O_2 molecule can be adsorbed on the bridge sites of neighboring Fe atoms in a vertical mode (Fe_2-N_6-O_2-ver, Fig. 4b, Supplementary Data 2). This adsorption configuration exhibits an E_{ads} of -2.913 eV and an O-O bond length of 1.336 Å. When the adsorbed O_2 takes the flat-lying bidentate configuration on neighboring Fe atoms in a parallel mode (Fe_2-N_6-O_2-par), the length of the O-O bond is stretched to 1.438 Å, while the adsorption is strengthened to -4.068 eV (Fig. 4c, Supplementary Data 3). As such, the most efficient activation of O_2 occurs on Fe_2-N_6 with the parallel mode considering the most negative E_{ads} and the longest of O-O bonds among these configurations.

To reveal the underlying mechanism from the perspective of electronic structures, we carried out spin-polarized project density of states (PDOS) analysis. As shown in Supplementary Fig. 53, the *d*-band center of Fe_2-N_6 (-1.48 eV) is much closer to the Fermi level than that of Fe_1-N_4 (-3.02 eV), signifying stronger chemisorption of Fe_2-N_6[32]. Furthermore, we analyzed Fe 3*d* and O 2*p* orbitals of Fe_1-N_4 and Fe_2-N_6 after oxygen adsorption, which is responsible for O_2 activation. The adsorbed O_2 on Fe_1-N_4 induces the formation of σ bonds which derives from the interaction of O 2*p* orbitals with the Fe $3d_{z^2}$ orbital (Fig. 4d). The O 2*p* and Fe 3*d* orbitals of Fe_2-N_6-O_2-ver exhibit a similar overlap to that of Fe_1-N_4-O_2 (Fig. 4e). As for Fe_2-N_6-O_2-par, the bonding interaction between O 2*p* and Fe $3d_{z^2}$ orbitals move away from Fermi level, indicating a weak σ bond (Fig. 4f). Moreover, the additional π bonds arise from the O 2*p*-Fe $3d_{x^2-y^2}$ hybridization on Fe_2-N_6 (Fig. 4f), accounting for the elevated charge density of oxygen atoms, leading to a strong interaction between O atoms and Fe atoms[33]. Therefore, neighboring Fe atoms favor parallel adsorption of O_2 which induces both σ bonds and π bonds.

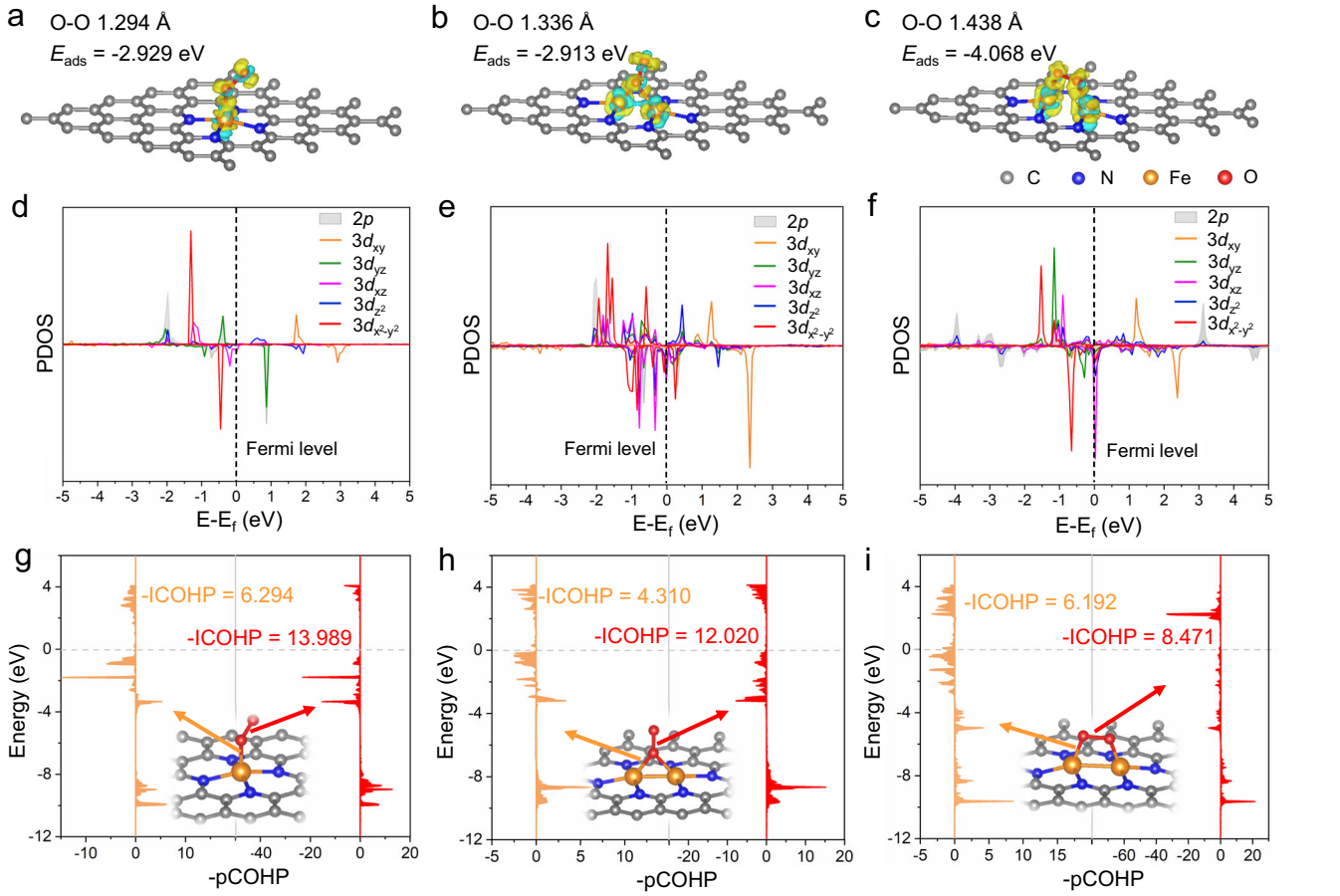

Fig. 4 | DFT studies. The charge density difference of (**a**) Fe_1-N_4-O_2, (**b**) Fe_2-N_6-O_2-ver, and (**c**) Fe_2-N_6-O_2-par, respectively. The isosurface value of the color region is 0.01 $Bohr^{-3}$. Yellow and cyan regions refer to the increased and decreased charge distribution, respectively. PDOS for Fe 3*d* orbitals and O 2*p* orbitals of (**d**) Fe_1-N_4-O_2, (**e**) Fe_2-N_6-O_2-ver, and (**f**) Fe_2-N_6-O_2-par. pCOHP of (**g**) Fe_1-N_4-O_2, (**h**) Fe_2-N_6-O_2-ver, and (**i**) Fe_2-N_6-O_2-par at different positions. The insets in panels **g**-**i** show the corresponding structures.

The bonding of O_2 with Fe atoms on Fe_1-N_4 and Fe_2-N_6 was further analyzed on the basis of crystal orbital Hamilton populations (COHP). The projected COHP profiles (pCOHP) for Fe-O bonds and O-O bond show the bonding (-pCOHP > 0) and anti-bonding (-pCOHP <0) interaction of O_2 adsorbed on Fe_1-N_4 and Fe_2-N_6 (Fig. 4g-i, Supplementary Fig. 54). Integrating the pCOHP to the Fermi level (E = 0 eV) gives the ICOHP which is a measure of bond strength. The -ICOHP value (6.192) of Fe-O bonds in Fe_2-N_6-O_2-par is between that (4.310) in Fe_2-N_6-O_2-ver and that (6.294) in Fe_1-N_4-O_2 (Fig. 4g-i), indicating a moderate interaction between O_2 and Fe atoms in Fe_2-N_6-O_2-par. Notably, Fe_2-N_6-O_2-par exhibits a much lower -ICOHP value (8.471) of O-O bond than that (12.020) in Fe_2-N_6-O_2-ver and that (13.989) in Fe_1-N_4-O_2 (Fig. 4g-i). As such, the O-O bond is significantly weakened when O_2 is parallelly adsorbed on neighboring Fe atoms, accounting for the facile oxygen activation.

Discussion

In summary, we demonstrated a general method for synthesizing neighboring M-N_x moieties with a specific pre-designed distance via an interfacial-fixing strategy. The precise preparation lies in the interfacial-fixing strategy where the distance between neighboring metal atoms relies on the crystal structure of the skeleton and the type of ligand. This work offers a top-down strategy to tune the distance between neighboring atoms, which is pre-designed instead of depending on the probability of metal loading. Precisely tuning the distance between neighboring metal atoms advances the fundamental understanding of single-atom catalysis.

Methods

Chemicals

All chemical reagents were used as received without further purification. Iron (III) chlorideanhydrous ($FeCl_3$; ≥ 99.9%), ammonium dihydrogen phosphate ($NH_4H_2PO_4$; ≥ 99.8%), tris (hydroxymethyl) aminomethane (≥ 99.9%), urea (≥ 99%), dopamine (≥ 98%), $Cu(NO_3)_2{\cdot}3H_2O$ (99.0 ~ 102.0%), $Co(NO_3)_2{\cdot}6H_2O$ (99%), $Ni(NO_3)_2{\cdot}6H_2O$ (≥ 98.5%), $Zn(NO_3)_2{\cdot}6H_2O$ (98%), $NaBH_4$ (98%), KOH (≥ 85%), $Zn(OAc)_2$ (≥ 99%), acrylamide (≥ 98%), N-N methylene bisacrylamide (≥ 99%), potassium persulfate (≥ 99.5%), dimethyl sulfoxide (≥ 99.5%), montmorillonite and $KMnO_4$ (≥ 99%) were obtained from Sinopharm Chemical Reagent Co. Ltd. Commercial Pt/C (20 wt%) catalyst was purchased from Sigma-Aldrich. Concentrated sulfuric acid (95.0 ~ 98.0%) and hydrochloric acid (36.0 ~ 38.0%) were purchased from Sinopharm Chemical Reagent (Shanghai, China). Deionized (DI) water was used throughout the experiments.

Synthesis of Fe_2O_3 nanotubes

Fe_2O_3 nanotubes were synthesized via a hydrothermal treatment, as described in[34]. Specifically, 14.0 mL of a 0.5 M $FeCl_3$ aqueous solution and 12.6 mL of a 0.02 M $NH_4H_2PO_4$ aqueous solution were mixed under vigorous stirring. Deionized (DI) water was then added to the mixture until the total volume reached 350 mL, followed by continued stirring for 10 minutes. The resulting mixture was transferred to a 500-mL Teflon-lined stainless-steel autoclave, and the hydrothermal reaction was conducted at 220 °C for 60 hours. After the reaction, the autoclave was allowed to cool naturally to room temperature. The red precipitates were then separated by centrifugation,

washed three times with DI water and ethanol, and dried at 80 °C under vacuum.

Synthesis of metallic Fe template with zero valence state

Metallic Fe with a zero-valence state was synthesized following the procedure outlined in ref. 35. First, 50 mg of $FeCl_3$ was dispersed in 50 mL of deionized water using ultrasonication for 30 minutes. Then, a freshly prepared aqueous $NaBH_4$ solution (50 mg of $NaBH_4$ in 50 mL of DI water) was added dropwise to the mixture under stirring, resulting in the formation of a black dispersion. The mixture was stirred continuously for 1 hour to ensure the complete reduction of the metal salt. Finally, the dispersion was filtered, washed five times with water, and dried in a vacuum oven at 60 °C overnight to yield the metallic Fe sample.

Synthesis of CuO, Co_3O_4, NiO, ZnO and MnO_2 templates

Carbonaceous microspheres (CMS) templates were synthesized via a hydrothermal method[36,37]. Metal precursors, including $Cu(NO_3)_2{\cdot}3H_2O$, $Co(NO_3)_2{\cdot}6H_2O$, $Ni(NO_3)_2{\cdot}6H_2O$, $Zn(NO_3)_2{\cdot}6H_2O$, and $KMnO_4$, were used to synthesize CuO, Co_3O_4, NiO, ZnO, and MnO_2 templates, respectively. In a typical procedure, 0.6 g of freshly prepared CMSs was dispersed in 50 mL of a 0.1 M precursor aqueous solution by ultrasonication for 30 minutes. The resulting suspension was allowed to stand for 6 hours, followed by vacuum filtration. The precipitate was washed three times with deionized water and then dried at 100 °C overnight. The resulting CMS-M (M = Cu, Co, Ni, Zn, Mn) composites were heated to 500 °C in air at a rate of 2 °C min^{-1}, maintained at 500 °C for 1 hour, and then cooled naturally. The hollow metal oxides, including CuO, Co_3O_4, NiO, ZnO, and MnO_2, were collected.

Synthesis of Fe_2-N_6

300.0 mg of Fe_2O_3 nanotubes were dispersed in 200.0 mL of freshly prepared tris-buffer solution (10 mM, pH 8.5) by ultrasonication for 1 h to form a suspension. Then 10.0 mL of urea (100.0 mg) and 20.0 mL of dopamine hydrochloride (310.0 mg) were added to the buffer solution. The mixed solution was stirred for 18 h at room temperature to finish the polymerization of dopamine, resulting in the formation of Fe_2O_3@polydopamine (Fe_2O_3@PDA). The resulting products were washed with DI water and ethanol three times and collected by centrifugation. After being dried at 80 °C, the Fe_2O_3@PDA was carbonized at 700 °C for 2 h under Ar atmosphere with a heating rate of 3 °C min^{-1} in a tube furnace. Then, the pyrolyzed products were etched with 4 M HCl solution for 72 h and further etched by 1 M H_2SO_4 for 12 h. Finally, 42 mg of double-layer hollow nanotubes containing Fe_2-N_6 was obtained after being filtered, washed with deionized water, and dried under vacuum. Following the same procedure, we synthesized the Fe_2-N_6-containing nanotubes with different thicknesses by adjusting the content of dopamine hydrochloride. Pure PDA nanoparticles were synthesized according to the same procedure without the addition of Fe_2O_3 seeds. After high-temperature treatment, nitrogen-doped carbon was achieved.

The sample yields were calculated as follows. In the synthesis process, 310 mg of dopamine hydrochloride was used as a polymer precursor for the synthesis of PDA layer that coated on the surface of hollow Fe_2O_3 tubes. After polymerization, pyrolysis and etching treatments, 42 mg of Fe_2-N_6 catalyst was obtained (2.36 wt% of Fe atoms anchored on double-layered carbon nanotubes), realizing a yield efficiency of ~13.2% (considered from the polymer precursor). Considering the etching process, we also calculated the yield of Fe during the synthesis. 300 mg of Fe_2O_3 nanotubes were used as a seed precursor for the preparation of Fe_2-N_6. Finally, 0.99 mg of Fe were fixed as single metal atoms that existed in Fe_2-N_6. As such, the yield of Fe atoms was only 0.33%. Although the majority of Fe atoms were etched by HCl, the obtained $FeCl_2$ and $FeCl_3$ could be re-used and oxidized to $FeCl_3$ aqueous solution. This solution was just the chemical reagent (Fe precursor) for the preparation of Fe_2O_3 hollow nanotubes, realizing the recycling of the Fe element.

Synthesis of Fe_2-N_6 with other ligands or different pyrolysis temperature

Fe_2-N_6 catalysts were also synthesized according the same procedure except for substituting urea with other ligands in terms of the same amount, such as thiourea and ethanediamine. Also, the Fe_2-N_6 catalysts were also synthesized by adjusting the amount of urea, as seen in supplementary Table S3. The usages of urea are 0, 10, 30, 50, 100 and 120 mg, respectively. Furthermore, Fe_2-N_6 catalyst with 50 mg of urea has also been produced at low temperature of 500 °C.

Synthesis of Fe_1-N_4

For comparison, double layer hollow nanotubes containing Fe_1-N_4 were prepared by the same procedure of Fe_2-N_6 except for adding urea.

Synthesis of Cu-N_x, Co-N_x, Ni-N_x, Zn-N_x, Mn-N_x moieties

For the preparation of Cu-N_x, Co-N_x, Ni-N_x, Zn-N_x, and Mn-N_x moieties, metal oxide nanomaterials (CuO, Co_3O_4, NiO, ZnO and MnO_2) were used as supporting templates, while PDA was coated on their surface with urea as an additional N resource. Specially, Cu_2O templates were synthesized according to a wet chemistry approach[38]. Co_3O_4, NiO, ZnO, and MnO_2 templates were synthesized according to the previously reported literature[39,40]. The following preparation processes including coating with PDA and urea, pyrolysis, as well as chemical etching are similar to that of Fe_2-N_6.

Synthesis of Fe moiety with ligand of ethanediamine and thiourea

Different ligands, including ethanediamine and thiourea, were also used to produce Fe moieties. The synthesis procedures were similar to that of Fe_2-N_6 except for using ethanediamine and thiourea to replace urea, respectively.

Acetylene TPD experiments

Temperature-programmed desorption (TPD) studies of acetylene were conducted utilizing a Micromeritics AutoChem II analyzer for chemisorption, connected to a Pfeiffer OmniStar mass spectrometer[41,42]. In a typical experiment, 50 mg of the sample was pre-treated with a 10% H_2/He mixture at 350 °C for a duration of 2 hours, then subjected to He purging at 300 °C for 1 hour. The sample was allowed to cool down to ambient temperature in a He atmosphere. After cooling, acetylene was admitted to the system to achieve saturation levels on the sample surface. A He purge at 25 °C was applied for 1 hour to remove any unreacted acetylene. The temperature was then elevated from 25 °C to 300 °C at a controlled rate of 10 °C per minute in a He flow, while concurrent acquisition of TPD spectra.

Characterizations

The crystallographic structure of prepared samples were determined by an XRD diffractometer (Bruker. D8 Advanced), scanning over an 2Theta range of 5 - 80° with Cu Kα radiation at a wavelength of 0.154056 nm. SEM images were carried out on a Hitachi SU8010 with a field emission gun, operating at an acceleration voltage of 5 kV. TEM images were characterized by a FEI Tecnai G2 F20. EDS detections were captured with a super-X detector with X-ray fluorescence emission system. XPS experiments were conducting using PHI QUANTUM2000 spectrometer. The iron concentration was quantified by ICP-OES on a Shimadzu ICPS-8100 instrument. HAADF-STEM was employed for the Fe_2-N_6 and Fe_1-N_4 catalysts, utilizing a JEOL JEM ARM300F microscope with a resolution capability of 0.063 nm. Nitrogen adsorption-desorption isotherms were measured with a Micrometrics ASAP 2020 system. The specific surface areas and pore

size distribution were calculated applying the BET equation and the nonlinear DFT model. The nitrogen content in the final Fe_2-N_6 sample was quantified using an Element Analyzer from UNICUBE in Germany.

Electrochemical measurements for ORR

RDE measurements. Electrochemical measurements were conducted utilizing a standard three-electrode system with a CHI760E electrochemical workstation (CH Instruments), complemented by a rotation apparatus from Pine Research Instrumentation. A glassy carbon disk electrode, procured from Pine Research Instrumentation in USA, functioned as the working electrode, and an Ag/AgCl (KCl, 3 M) electrode served as the reference. A platinum wire fulfilled the role of the counter electrode. Reported potentials are referenced to the standard reversible hydrogen electrode (RHE).

For the preparation of the working electrode, a mixture of 2 mg of the sample and 5 μL of a 5 wt% Nafion solution in 400 μL of ethanol was sonicated for 1 hour to achieve a homogeneous ink. Then, 10 μL of this ink was pipetted onto a glassy carbon electrode with a diameter of 5 mm, resulting in a catalyst mass loading of 0.255 mg cm^{-2}. As a compared sample, 2 mg of Pt/C was dispersed in 400 μL of ethanol along with 5 μL of the 5 wt% Nafion solution, and applying 10 μL to a glassy carbon electrode. The inks were allowed to dry at room temperature to ensure an uniform distribution across the electrode surface.

Electrochemical experiments were executed in an O_2-saturated 0.1 M KOH aqueous electrolyte. Cyclic voltammetry (CV) measurements were performed at a scan rate of 50 mV s^{-1}. Linear sweep voltammetry (LSV) curves were recorded by using a rotating disk electrode (RDE) with a rotation speed of 1600 rpm and a scan rate of 10 mV s^{-1}. LSV polarization curves were derived at various rotation speeds ranging from 400 to 2500 rpm, with background currents being corrected using data from Ar-saturated electrolyte. To assess the stability of the oxygen reduction reaction (ORR), an accelerated durability test (ADT) was conducted at potential of 0.6 V and 1.2 V, with a scan rate of 100 mV s^{-1} over 50,000 cycles. Following this, the ORR steady-state polarization curves were obtained in the O_2-saturated 0.1 M KOH solution. The methanol tolerance of samples was assessed by introducing 2 mL of methanol into the electrolyte at 500 seconds mark of the chronoamperometric measurements.

The applied potential relative to Ag/AgCl (KCl, 3 M) is converted to the reversible hydrogen electrode (RHE) potential using the following equation:

$$E_{RHE} = E_{Ag/AgCl} + 0.059pH + E^{\circ}_{Ag/AgCl} \quad (1)$$

where $E_{Ag/AgCl}$ was the experimentally measured potential using Ag/AgCl as the reference electrode and $E^{\circ}_{Ag\ /\ AgCl}$ was 0.199 V.

The number of electrons transferred (n) was calculated according to the K-L equation:

$$\frac{1}{J} = \frac{1}{J_L} + \frac{1}{J_K} = \frac{1}{B\omega^{\frac{1}{2}}} + \frac{1}{J_K} \quad (2)$$

$$B = 0.62\, n F\, C_0 (D_0)^{2/3} \nu^{-1/6} \quad (3)$$

$$J_K = n F\, k\, C_0 \quad (4)$$

J, J_K and J_L represent the current density, the kinetic and diffusion-limiting current densities, respectively. The angular velocity of the rotating electrode is defined as $\omega = 2\pi N$, where N is the linear rotation speed. F refers to the Faraday constant, which is 96485 C mol^{-1}. The concentration of O_2 in 0.1 M KOH is given as $C_0 = 1.2\times10^{-6}$ mol cm^{-3}, and the diffusion coefficient of O_2 in this solution is $D_0 = 1.9\times10^{-5}$ cm^2 s^{-1}. Additionally, ν denotes the kinematic viscosity of the electrolyte, with a value of 0.01 cm^2 s^{-1}, and k represents the electron transfer rate constant. Electrochemical impedance spectroscopy (EIS) tests were performed over a frequency range from 100 kHz to 100 mHz, using an amplitude of 5 mV to facilitate IR correction.

Catalytic activity comparison between Fe_1-N_4 and Fe_2-N_6

In order to make a comparison between the catalytic activities of Fe_1-N_4 and Fe_2-N_6 samples, we mixed Fe_2-N_6 with the C-N matrix in an electrode to ensure the same content of Fe atoms in the prepared electrode as that in Fe_1-N_4. For Fe_1-N_4, 2 mg of the sample (0.32 wt% Fe) and 5 μL of Nafion solution (5 wt%) were dispersed in 400 μL of ethanol solution by sonication for 1 h to form a homogeneous ink. Next, 10 μL of the catalyst dispersion was pipetted onto a glassy carbon electrode with a diameter of 5 mm. The Fe content in this electrode was 1.6×10^{-4} mg. For Fe_2-N_6, 0.678 mg of the sample (2.36 wt%) and 4.32 mg of C-N sample were mixed with 12 μL of Nafion solution in 1000 μL of ethanol solution by sonication for 1 h to form homogeneous ink. Next, 10 μL of the catalyst dispersion was pipetted onto a glassy carbon electrode with a diameter of 5 mm. The mixed catalyst was denoted as Fe_2-N_6/C-N. As such, the Fe content in this electrode was also 1.6×10^{-4} mg, equal to that of the electrode containing Fe_1-N_4. And the electrochemical analysis was the same as RDE measurements mentioned above.

RRDE measurements

Catalyst inks and electrodes were prepared as aforementioned in RDE measurements The disk electrode underwent cathodic polarization at a linear sweep rate of 5 mV s^{-1}, with the ring electrode held at a fixed potential of 0.5 V versus Ag/AgCl. The data gleaned from the rotating ring-disk electrode (RRDE) studies facilitated the calculation of $HO2^-$ yield and the electron transfer number (n), employing the following equations.

$$n = \frac{4\times i_d}{i_d + \frac{i_r}{N}} \quad (5)$$

$$HO_2^-\% = \frac{200\times \frac{i_r}{N}}{i_d + \frac{i_r}{N}} \quad (6)$$

where i_d and i_r denote the disk current and the ring current, respectively. And N represents the current collection efficiency of the Pt ring with a value of 0.37, which was provided by the manufacturer.

CO-tolerance experiments

The tolerance of Fe_2-N_6 to CO compared with those of Fe_1-N_4 and Pt/C (20%) electrocatalyst was carried out by the chronoamperometric response at 0.1 V for the three electrodes. CO (v/v = 1:9, CO/O_2) was introduced into the O_2-saturated 0.1-M KOH electrochemical cell at 1550 s. Afterwards, the response of current density was recorded for another 8450 s.

XAFS measurements

Data pertaining to X-ray absorption fine structure (XAFS) at the Fe K-edge were acquired at the BL14W1 beamline of the Shanghai Synchrotron Radiation Facility (SSRF), which functions at an energy of 3.5 GeV with a constant current of 220 mA, operating in "top-up" mode. The XAFS measurements were performed in fluorescence mode, using a 32-element Ge solid-state detector array. The energy calibration was referenced against the absorption edge of pure Fe powder. The Athena and Artemis software packages were used for data extraction and profile fitting.

For X-ray absorption near-edge structure (XANES) analysis, the experimental absorption coefficients, represented as a function of energy, μ(E), underwent background removal and normalization to yield "normalized absorption" spectra. For the extended X-ray

absorption fine structure (EXAFS) analysis, the data were subjected to Fourier-transformed (FT) to obtain the radial distribution in R space. This analysis was conducted using either a first-shell approximation or a metallic Fe model to account for Fe-O and Fe-Fe scattering paths. The passive electron factor (S_0^2) was ascertained by fitting the Fe foil data, with the coordination number (CN) of the Fe-Fe shell fixed to enable further analysis of the measured samples. The fitting process allowed for the variation of parameters describing the electronic properties (such as the correction to the photoelectron energy origin, E_0), as well as the local structural environment, including CN, bond distance (R), and Debye-Waller factor (σ^2) around the absorbing atoms.

Assembly of Zn-air batteries

All the electrochemical performance of Zn-air batteries was evaluated in home-built electrochemical devices. Fe_2-N_6 catalyst ink was loaded on a PTFE-treated porous carbon paper ($1 \times 1\,cm^2$) and further used as the air cathode. A polished zinc foil was utilized as the anode. 6 M KOH aqueous solution with 0.2 M zinc acetate was used as the electrolyte. Polarization curves and galvanostatic discharge tests were carried out on an electrochemical workstation (CHI 760E) and LAND testing systems. Amount of catalysts used in cathode was 0.25 mg cm^{-2} for Fe_2-N_6, Fe_1-N_4 and commercial Pt/C.

Assembly of flexible solid-state Zn-air batteries

A polished zinc plate was used as anode, 6 M KOH + 0.2 M $Zn(OAc)_2$ filled PAM/MMT organic hydrogel was used as solid electrolyte and Arc-Co SAC or Pt/C+Ir/C catalyst on carbon cloth was used as the air cathodes. To form the solid polymer electrolyte, 5 g acrylamide (AM), 5 mg N-N methylene bisacrylamide (MBA), and 12.5 mg potassium persulfate (KPS) were added into 20 mL mixed solvent of deionized water and dimethyl sulfoxide (DMSO) (1:1, water: DMOS). The mixed solution was stirred for 30 min before 15 mg montmorillonite (MMT) was added and the obtained mixture was kept stirring for 30 min. The obtained gel was moved to the mold and the polymerization was occurred at 60 °C for 16 h. After cooling process, the obtained PAM/MMT organic hydrogel was immersed in 6 M KOH + 0.2 M $Zn(OAc)_2$ solution for 72 h before used. To package the flexible solid Zn-Air battery, carbon cloth that coated with catalyst and the polished zinc plate were placed on opposite sides of the polymer electrolyte film. All tests for the flexible solid Zn-Air battery were performed on the LAND-CT2001A test system (Land). A cycling test was performed using recurrent galvanostatic pulses for 10 min of discharge, followed by 10 min of charge. And for the large current density, the discharge and charge time were changed to 20 min.

DFT calculations

All density functional theory (DFT) calculations were implemented using the Vienna Ab initio Simulation Package (VASP)[43]. The generalized gradient approximation (GGA) with Perdew-Burke-Ernzerhof (PBE) functional and the projector augmented wave (PAW) potential were used to describe the exchange-correlation energy and the electron-ion interaction, respectively[44,45]. The DFT-D3 empirical correction method was employed to accurately describe the van der Waals interaction[46]. The Fe_1-N_4 model contains a Fe atom, four nitrogen atoms and forty-four carbon atoms in a supercell, and Fe_2-N_6 model contains two Fe atoms, six nitrogen atoms and forty carbon atoms. The convergence of energy and forces were 1×10^{-5} eV and 0.005 eV·Å^{-1}, respectively. The cut-off energy for the plane wave basis set is 500 eV. Γ-centered k-grids of 5×5×1 and 17×17×1 with the Monkhorst-Pack scheme are used in geometry optimizations and electronic-structure calculations, respectively[47]. The adsorption energy (E_a) was calculated according to the following equation:

$$E_a = E_{total} - E_{substrate} - E_{O_2} \quad (7)$$

where E_{total}, $E_{substrate}$ and E_{O2} are the energies of O_2 absorbed on matrix, Fe single atom matrix or adjacent Fe single atom matrix, and O_2, respectively. The charge difference for substrate-adsorbate hybrids can be determined using the following equation:

$$\Delta\rho = \rho_{\text{total}} - \rho_{\text{substrate}} - \rho_{O_2} \quad (8)$$

where ρ_{total}, $\rho_{\text{substrate}}$, and ρ_{O2} correspond to the charge density of substrate after O_2 adsorption, charge density of pure substrate and change density of O_2, respectively.

Data availability

The data that support the findings of this study are available from the corresponding author upon reasonable request. Source data are provided with this paper.

References

1. Collman, J. P. et al. A Cytochrome c Oxidase Model Catalyzes Oxygen to Water Reduction Under Rate-Limiting Electron Flux. *Science* **315**, 1565–1568 (2007).
2. Cao, X. et al. Atomic Bridging Structure of Nickel–Nitrogen–Carbon for Highly Efficient Electrocatalytic Reduction of CO_2. *Angew. Chem. Int. Ed.* **61**, e202113918 (2022).
3. Fu, J. et al. Synergistic Effects for Enhanced Catalysis in a Dual Single-Atom Catalyst. *ACS Catal.* **11**, 1952–1961 (2021).
4. Wang, Y. et al. Flexible carbon nanofiber film with diatomic Fe-Co sites for efficient oxygen reduction and evolution reactions in wearable zinc-air batteries. *Nano Energy* **87**, 106147 (2021).
5. Li, H. et al. Synergetic interaction between neighbouring platinum monomers in CO_2 hydrogenation. *Nat. Nanotech.* **13**, 411–417 (2018).
6. Liu, P. et al. Photochemical route for synthesizing atomically dispersed palladium catalysts. *Science* **352**, 797–800 (2016).
7. Cao, S. et al. High-loading single Pt atom sites [Pt-O(OH)$_x$] catalyze the CO PROX reaction with high activity and selectivity at mild conditions. *Sci. Adv.* **6**, eaba3809.
8. Zhou, Y. et al. Dual-Metal Interbonding as the Chemical Facilitator for Single-Atom Dispersions. *Adv. Mater.* **32**, 2003484 (2020).
9. Bai, L., Hsu, C.-S., Alexander, D. T. L., Chen, H. M. & Hu, X. A Cobalt–Iron Double-Atom Catalyst for the Oxygen Evolution Reaction. *J. Am. Chem. Soc.* **141**, 14190–14199 (2019).
10. Ding, T. et al. Atomically Precise Dinuclear Site Active toward Electrocatalytic CO_2 Reduction. *J. Am. Chem. Soc.* **143**, 11317–11324 (2021).
11. Zhang, X. et al. Platinum–copper single atom alloy catalysts with high performance towards glycerol hydrogenolysis. *Nat. Commun.* **10**, 5812 (2019).
12. Han, A. et al. An Adjacent Atomic Platinum Site Enables Single-Atom Iron with High Oxygen Reduction Reaction Performance. *Angew. Chem. Int. Ed.* **60**, 19262–19271 (2021).
13. Chukwu, E. & Yang, M. Uncertainties in the reactivity of atomically dispersed catalytic metal: Can any single-atom catalyst work like a charm? *Chem Catal.* **3** (2023).
14. Hai, X. et al. Scalable two-step annealing method for preparing ultra-high-density single-atom catalyst libraries. *Nat. Nanotech.* **17**, 174–181 (2022).
15. Xia, C. et al. General synthesis of single-atom catalysts with high metal loading using graphene quantum dots. *Nat. Chem.* **13**, 887–894 (2021).
16. Wang, J. et al. Design of N-Coordinated Dual-Metal Sites: A Stable and Active Pt-Free Catalyst for Acidic Oxygen Reduction Reaction. *J. Am. Chem. Soc.* **139**, 17281–17284 (2017).
17. Li, J. et al. Modulating the Electronic Coordination Configuration and d-Band Center in Homo-Diatomic Fe_2N_6 Catalysts for Enhanced

Peroxymonosulfate Activation. *ACS Appl. Mater. Interfaces* **14**, 37865–37877 (2022).
18. Hao, Q. et al. Nickel dual-atom sites for electrochemical carbon dioxide reduction. *Nat. Synth.* **1**, 719–728 (2022).
19. Zhu, C. et al. Hierarchically Porous M–N–C (M = Co and Fe) Single-Atom Electrocatalysts with Robust MN Active Moieties Enable Enhanced ORR Performance. *Adv. Energy Mater.* **8**, 1801956 (2018).
20. Han, L. et al. Modulating Single-Atom Palladium Sites with Copper for Enhanced Ambient Ammonia Electrosynthesis. *Angew. Chem. Int. Ed.* **60**, 345–350 (2021).
21. Wei, Y.-S. et al. Fabricating Dual-Atom Iron Catalysts for Efficient Oxygen Evolution Reaction: A Heteroatom Modulator Approach. *Angew. Chem. Int. Ed.* **59**, 16013–16022 (2020).
22. Jiao, L. et al. Non-Bonding Interaction of Neighboring Fe and Ni Single-Atom Pairs on MOF-Derived N-Doped Carbon for Enhanced CO_2 Electroreduction. *J. Am. Chem. Soc.* **143**, 19417–19424 (2021).
23. Zhang, M. et al. Metal (Hydr)oxides@Polymer Core–Shell Strategy to Metal Single-Atom Materials. *J. Am. Chem. Soc.* **139**, 10976–10979 (2017).
24. Liu, M. et al. A "Pre-Constrained Metal Twins" Strategy to Prepare Efficient Dual-Metal-Atom Catalysts for Cooperative Oxygen Electrocatalysis. *Adv. Mater.* **34**, 2107421 (2022).
25. Jin, Z. et al. Understanding the inter-site distance effect in single-atom catalysts for oxygen electroreduction. *Nat. Catal.* **4**, 615–622 (2021).
26. Gu, H. et al. Adjacent single-atom irons boosting molecular oxygen activation on MnO_2. *Nat. Commun.* **12**, 5422 (2021).
27. Jiao, J. et al. Copper atom-pair catalyst anchored on alloy nanowires for selective and efficient electrochemical reduction of CO_2. *Nat. Chem.* **11**, 222–228 (2019).
28. Wan, J. et al. In Situ Phosphatizing of Triphenylphosphine Encapsulated within Metal–Organic Frameworks to Design Atomic Co-P_1N_3 Interfacial Structure for Promoting Catalytic Performance. *J. Am. Chem. Soc.* **142**, 8431–8439 (2020).
29. Pacilé, D. et al. Electronic properties and atomic structure of graphene oxide membranes. *Carbon* **49**, 966–972 (2011).
30. Wang, M. et al. Non-planar Nest-like [Fe_2S_2] Cluster Sites for Efficient Oxygen Reduction Catalysis. *Angew. Chem. Int. Ed.* **62**, e202300826 (2023).
31. Zhang, S., Qin, Y., Ding, S. & Su, Y. A DFT Study on the Activity Origin of Fe–N–C Sites for Oxygen Reduction Reaction. *ChemPhysChem* **23**, e202200165 (2022).
32. Xin, H., Vojvodic, A., Voss, J., Nørskov, J. K. & Abild-Pedersen, F. Effects of d-band shape on the surface reactivity of transition-metal alloys. *Phys. Rev. B* **89**, 115114 (2014).
33. Shang, H. et al. Engineering unsymmetrically coordinated Cu-S_1N_3 single atom sites with enhanced oxygen reduction activity. *Nat. Commun.* **11**, 3049 (2020).
34. Fan, H. M. et al. Shape-Controlled Synthesis of Single-Crystalline Fe_2O_3 Hollow Nanocrystals and Their Tunable Optical Properties. *J. Phys. Chem. C.* **113**, 9928–9935 (2009).
35. Guo, J., Wang, R., Tjiu, W. W., Pan, J. & Liu, T. Synthesis of Fe nanoparticles@graphene composites for environmental applications. *J. Hazard. Mater.* **225–226**, 63–73 (2012).
36. Lai, X. et al. General Synthesis and Gas-Sensing Properties of Multiple-Shell Metal Oxide Hollow Microspheres. *Angew. Chem. Int. Ed.* **50**, 2738–2741 (2011).
37. Wang, J. et al. Multi-shelled metal oxides prepared via an anion-adsorption mechanism for lithium-ion batteries. *Nat. Energy* **1**, 16050 (2016).
38. Fang, Y., Luan, D., Chen, Y., Gao, S. & Lou, X. W. D. Rationally Designed Three-Layered Cu_2S@Carbon@MoS_2 Hierarchical Nanoboxes for Efficient Sodium Storage. *Angew. Chem. Int. Ed.* **59**, 7178–7183 (2020).
39. Wang, J. et al. Accurate Control of Multishelled Co_3O_4 Hollow Microspheres as High-Performance Anode Materials in Lithium-Ion Batteries. *Angew. Chem. Int. Ed.* **52**, 6417–6420 (2013).
40. Wang, J., Wan, J. & Wang, D. Hollow Multishelled Structures for Promising Applications: Understanding the Structure–Performance Correlation. *Acc. Chem. Res.* **52**, 2169–2178 (2019).
41. Gu, J. et al. Synergizing metal–support interactions and spatial confinement boosts dynamics of atomic nickel for hydrogenations. *Nat. Nanotech.* **16**, 1141–1149 (2021).
42. Zhang, Z. et al. Atomically Dispersed Cobalt Trifunctional Electrocatalysts with Tailored Coordination Environment for Flexible Rechargeable Zn–Air Battery and Self-Driven Water Splitting. *Adv. Energy Mater.* **10**, 2002896 (2020).
43. Kresse, G. & Hafner, J. Ab initio molecular dynamics for open-shell transition metals. *Phys. Rev. B* **48**, 13115–13118 (1993).
44. Perdew, J. P., Burke, K. & Ernzerhof, M. Generalized Gradient Approximation Made Simple. *Phys. Rev. Lett.* **77**, 3865–3868 (1996).
45. Blöchl, P. E. Projector augmented-wave method. *Phys. Rev. B* **50**, 17953–17979 (1994).
46. Grimme, S., Antony, J., Ehrlich, S. & Krieg, H. A consistent and accurate ab initio parametrization of density functional dispersion correction (DFT-D) for the 94 elements H-Pu. *J. Chem. Phys.* **132**, 154104 (2010).
47. Monkhorst, H. J. & Pack, J. D. Special points for Brillouin-zone integrations. *Phys. Rev. B* **13**, 5188–5192 (1976).

Acknowledgements

The authors acknowledge the fund support of the National Key Research and Development Program of China (2021YFA1500500, 2023YFA1508003), CAS Project for Young Scientists in Basic Research (YSBR-051), National Science Fund for Distinguished Young Scholars (21925204), NSFC (22475003, 22479001, 22221003, 22250007, 22308346, 22209063), the DNL Cooperation Fund, CAS (DNL202003), Anhui National Science Fund for Distinguished Young Scholars (2308085J16, 2408085J008), the Key Research and Development Program of Xuzhou (KC22497), the Natural Science Foundation of Xuzhou City (KC21283), the Priority Academic Program Development of Jiangsu Higher Education Institutions, the Postgraduate Research and Practical Innovation Program of Jiangsu Province (KYCX20_2230), the Joint Fund of the Yulin University and the Dalian National Laboratory for Clean Energy (YLU-DNL Fund 2022012), Joint Funds from the Hefei National Synchrotron Radiation Laboratory (KY9990000202), Natural Science Foundation of Anhui Province (2208085QB42), the State Key Laboratory of Catalysis (2024SKL-A-01), and USTC Research Funds of the Double First-Class Initiative (YD9990002014). J.Z. acknowledges support from the New Cornerstone Science Foundation through the XPLORER PRIZE. This work was partially carried out at the Instruments Center for Physical Science, University of Science and Technology of China. This work was also partially carried out at the USTC Center for Micro and Nanoscale Research and Fabrication.

Author contributions

Y.Y., M.L., H.L., and J.Z. designed the studies and wrote the paper. Y.Y., R.Y., and M.L. synthesized catalysts. M.L., Z.Q., J.Y., and H.L. performed catalytic tests. M.L., S.H., and H.L. conducted characterizations. Y.Y. contributed to DFT calculations. All authors discussed the results and commented on the manuscript.

Competing interests

The authors declare no competing interests.

Additional information

Supplementary information The online version contains supplementary material available at https://doi.org/10.1038/s41467-024-55630-y.

Correspondence and requests for materials should be addressed to Mingkai Liu, Hongliang Li or Jie Zeng.

Peer review information *Nature Communications* thanks Jin-Song Hu, and the other, anonymous, reviewer(s) for their contribution to the peer review of this work. A peer review file is available.

Reprints and permissions information is available at http://www.nature.com/reprints

Publisher's note Springer Nature remains neutral with regard to jurisdictional claims in published maps and institutional affiliations.

Open Access This article is licensed under a Creative Commons Attribution-NonCommercial-NoDerivatives 4.0 International License, which permits any non-commercial use, sharing, distribution and reproduction in any medium or format, as long as you give appropriate credit to the original author(s) and the source, provide a link to the Creative Commons licence, and indicate if you modified the licensed material. You do not have permission under this licence to share adapted material derived from this article or parts of it. The images or other third party material in this article are included in the article's Creative Commons licence, unless indicated otherwise in a credit line to the material. If material is not included in the article's Creative Commons licence and your intended use is not permitted by statutory regulation or exceeds the permitted use, you will need to obtain permission directly from the copyright holder. To view a copy of this licence, visit http://creativecommons.org/licenses/by-nc-nd/4.0/.

© The Author(s) 2025